THE JOURNAL OF PHYSICAL CHEMISTRY C
A JOURNAL OF THE AMERICAN CHEMICAL SOCIETY

pubs.acs.org/JPCC

Article

Electron Paramagnetic Resonance Quantifies Hot-Electron Transfer from Plasmonic Ag@SiO_2 to $Cr^{6+}/Cr^{5+}/Cr^{3+}$

Constantinos Moularas, Christos Dimitriou, Yiannis Georgiou, Georgios Evangelakis, Nikos Boukos, and Yiannis Deligiannakis*

Cite This: *J. Phys. Chem. C* 2023, 127, 2045−2057

Read Online

ACCESS | Metrics & More | Article Recommendations | Supporting Information

ABSTRACT: Understanding the plasmon-mediated electron-transfer mechanisms from plasmonic nanostructures to redox-active metals is a technically challenging and still developing procedure. Electron paramagnetic resonance (EPR) spectroscopy is well established as a state-of-the-art tool to selectively detect the redox evolution of paramagnetic metals; however, its use in plasmon-driven charge-transfer processes has not been explored so far. Herein, we present a quantitative study on the mechanism of hot-electron transfer, from plasmonic Ag@SiO_2 nanoaggregates, to drive sequential Cr^{6+} reduction toward Cr^{5+}/Cr^{3+}. Employing flame spray pyrolysis (FSP), core−shell Ag@SiO_2 nanoaggregates were engineered with varying SiO_2-shell thickness, in the range of 1−5 nm. Using EPR spectroscopy, the spin Hamiltonian parameters for the $S = 1/2$ {oxalate-Cr^{5+}} and $S = 3/2$ {oxalate-Cr^{3+}} systems at the Ag@SiO_2/Cr interface are analyzed and used to quantitatively monitor the sequential electron-transfer steps during Cr^{6+} reduction. In the absence of the SiO_2 shell, the oxidative path via the dark reduction of Cr^{6+} due to the oxidation of bare Ag was deducted accordingly. Importantly, we show that the SiO_2 shell plays a key role in hot-electron transfer, as the 1 nm shell allows a predominant hot-electron transfer via a light-induced decrease of the activation barrier, suppressing the oxidative path and excluding photothermal effects.

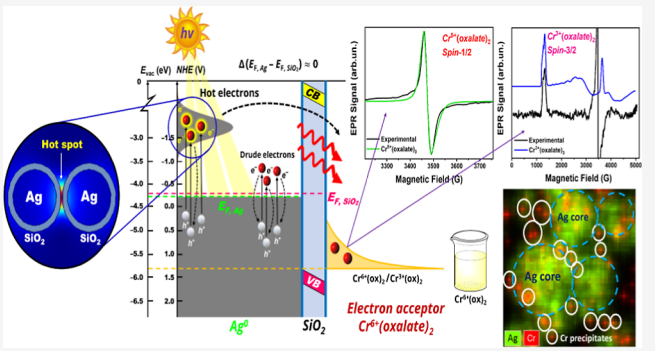

1. INTRODUCTION

Remediation of hexavalent chromium Cr^{6+} in environmental water sources is a key priority to assure the protection of public health.[1] So far, the most efficient route of Cr^{6+} removal is the reduction to the inert trivalent chromium Cr^{3+}, with the photocatalytic reduction route being the most effective, low-cost, and hazardous-free procedure.[2] During the last decade, metal nanoparticles have emerged as highly potent, promising photocatalysts, and plasmon-assisted photochemistry is considered the next step in boosting challenging solar-to-chemical processes.[3−6] However, the evaluation of plasmonic photocatalysts in Cr^{6+} removal using solar light remains to be investigated.

In particular, the excitation of local surface plasmon resonance (LSPR) phenomenon drives two distinct mechanisms: Upon irradiation, surface plasmons form and decay,[7,8] initiating either [i] heat generation *via* thermal relaxation of photoinduced carriers[9,10] or [ii] energetic "hot" electron transfer to an appropriate acceptor.[11,12] So far, there is converging evidence that hot electrons, despite their short lifetime, can be efficiently utilized in challenging chemical processes of immediate technological importance, such as H_2 production[13−15] and CO_2 reduction,[16−18] to name a few.

So far, however, the transfer of hot electrons to redox-active metals has not been thoroughly addressed. An interesting case is hexavalent Cr^{6+}, since its reduction to Cr^{3+} is the key-technology to remediate its toxicity. Detection of the hot-carrier transfer in {plasmonic}-{electron-acceptor} interfaces is—by itself—a primary challenge, both from the technical point of view by establishing a widely useable technique for quantitative monitoring of hot electrons in such systems as well as from the theoretical point of view by understanding/disentangling which mechanism predominates among plasmonic excitation, hot-electron generation, thermal dissipation, and near fields. Transferring these to realistic, non-monodispersed nanoaggregates is also a forward-looking realm.

Based on estimates from ultrafast kinetics/non-equilibrium studies so far, we understand that key factors that determine the transfer efficiency of hot electrons to a nearby acceptor can be conceptually separated as [i] processes occurring inside the

Received: November 7, 2022
Revised: December 17, 2022
Published: January 19, 2023

https://doi.org/10.1021/acs.jpcc.2c07837
J. Phys. Chem. C 2023, 127, 2045−2057

metallic particle, that is, photoexcitation of plasmon modes, hot-carrier generation and relaxation and [ii] factors related to the particle−acceptor interface, that is, the probability of the hot electron reaching the particle surface and being injected into the acceptor. Typically, processes [i] are transient, characterized by ultrafast kinetics, while phenomena in [ii] tend to relate to equilibrium states. In this case, interfacial or quasi-equilibrium reactions are the slowest; thus, they determine the rate-limiting steps of the entire process. However, a quantitative capturing and monitoring of plasmon-induced hot electrons under chemical equilibrium remains highly challenging. Seemala et al. have demonstrated that Ag nanoparticles can achieve plasmon-mediated O_2 dissociation, with the dominant mechanism assigned to intense surface electric fields, while the hot carriers had no effect on this particular reaction.[19] In monodisperse spherical Ag nanoparticles, the theoretical hot-electron lifetime is in the range of picoseconds, while the optimal range of particle size for maximizing the hot-electron yield lies between 10 and 20 nm.[20] In practical applications, where non-monodisperse nanoaggregates are often used, tuning the interparticle distance (plasmonic coupling) through the aggregation degree, promotes the generation of hot carriers due to enhanced electric fields localized between neighboring particles.[21−23] Thus, in the case of a non-monodispersed Ag nanoensemble, the hot-electron generation rate becomes both size- and aggregation-dependent.[24]

In this context, the development of an appropriate method for monitoring the generation and harvesting of hot carriers still poses a challenge by itself. The methods used so far can be classified as (i) fast-kinetic spectroscopies, reviewed by Hartland[10] and Besteiro et al.,[25] (ii) imaging methods,[26−32] or (iii) monitoring the products of a selected chemical process. Despite the first two methods providing a fundamental understanding of the process, approach (iii) is of key importance to understand the process under chemical equilibrium. However, despite the great progress achieved so far,[33−36] direct quantitative monitoring of the energetic carriers remains elusive. Herein, we have used electron paramagnetic resonance (EPR) as a state-of-the-art spectroscopy to study the transfer of hot electrons from photoexcited core−shell Ag@SiO_2 nanoaggregates to Cr^{6+}-atoms. {Cr-oxalate} is employed as a well-studied, electron-accepting system.[37−40] One-electron reduction of Cr^{6+} results in Cr^{5+} (1a), and a subsequent two-electron reduction of Cr^{5+} results in Cr^{3+} formation (1b)

$$Cr^{6+} + e^-_{hot} \rightarrow Cr^{5+} \quad (1a)$$

$$Cr^{5+} + 2e^-_{hot} \rightarrow Cr^{3+} \quad (1b)$$

In the presence of illuminated Ag@SiO_2 nanoaggregates, the overall electron transfer is described by reaction 2 as

$$Ag^0@SiO_2 + h\nu + Cr^{6+} \xrightarrow{e^-_{hot}} Cr^{5+} \xrightarrow{2e^-_{hot}} Cr^{3+} \quad (2)$$

Hence, quantitative monitoring of the {Cr^{6+}-, Cr^{5+}-, and Cr^{3+}-oxalate} species offers complete mass balance control, which allows direct electron counting.

EPR is eminently suited to detect and quantify unpaired electrons in metal centers,[41,42] as well as unpaired spins in small Ag nanoparticles[43,44] and photo-induced trapped carriers.[45] Quantitative EPR analysis should take into account the spin state of the studied system.[41,42] More specifically, for $S > 1/2$ systems, the work of Chasteen had clearly exemplified the way to quantify EPR signals for high-spin Fe^{3+} ($S = 5/2$).[46] Herein, we use the spin Hamiltonian for the $S = 3/2$ {Cr^{3+}-oxalate} system, and we account for a spin-state-corrected spin quantitation protocol. In the same context, the $S = 1/2$ {Cr^{5+}-oxalate} system was analyzed and spin-quantified. In this way, we use EPR spectra as quantitative indexes of the number of electrons transferred to Cr-species according to reactions 1a and 1b.

The plasmonic $Ag^0@SiO_2$ nanoaggregates studied herein were synthesized using flame spray pyrolysis (FSP), whose photothermal profile has been thoroughly characterized in our previous work.[47] Ag is the chosen material here since it displays superior plasmon resonance in the optical region and thus the capability to excite higher energetic carriers.[48] Herein, three core@shell $Ag^0@SiO_2$ configurations were employed (see Table S1), with a 15 nm Ag core and varying the SiO_2 thickness to 1−5 nm. The encapsulation of Ag particles by a SiO_2 shell has been proven beneficial, as it (i) protects the Ag core from oxidation, (ii) hinders the leaching of Ag ions,[49] and (iii) provides a friendly surface for interfacial chemistry.[43] Using EPR spectroscopy, we establish a spin-state-calibrated EPR methodology to quantitatively monitor the multi-electron transfer steps from photoexcited Ag@SiO_2 toward the reduction of {oxalate-Cr^{6+}} to {oxalate-Cr^{5+}/Cr^{3+}} species, respectively. Moreover, in such a quantitative study, it was important to assess the possible direct Cr^{6+} reduction that is due to the oxidation of the non-coated Ag surface. Thus, using FSP, we have synthesized non-coated Ag particles that were simply deposited on SiO_2. We show that in core@shell Ag@SiO_2, the SiO_2 shell plays a key role in hot-electron generation and migration. In a wider context, the present study exemplifies the possibility of plasmon-enhanced reduction of toxic Cr^{6+} ions toward inert Cr^{3+} within the picture of environmental chromium remediation.

2. EXPERIMENTAL METHODS

2.1. FSP Synthesis of Ag Particles. The nanoparticles were synthesized using a FSP setup, as already reported.[47] The precursor solution was prepared by dissolving silver acetate (Sigma-Aldrich, purity >99%) in 2-ethylhexanoic acid (EHA) and acetonitrile (ACN) (both from Sigma-Aldrich, purity >97%) in a volume ratio of 1:1 at varying concentrations of 0.4−0.5 M. Then, the solution was fed through a capillary at 5−7 mL min^{-1} into the flame and atomized into fine droplets by 5 L min^{-1} dispersed O_2 (Linde, purity >99%). Pressure drop at the nozzle tip was maintained at 1.5 bar. A supporting O_2/CH_4 (5, 2.5 L min^{-1}) pilot flame ignites the droplets, initiates combustion, and supports the spray flame. The high temperature inside the flame field triggers the metal vapor to form nuclei through the desired gas-to-particle formation.[50,51] Particle coalescence, sintering, and agglomeration result in the final powder being collected using a vacuum pump (Busch V40) on glass microfiber filters (Albet). Nanoparticles were collected by scraping the powder from the filter.

2.2. Synthesis of Core@Shell Ag@SiO_2. The *in situ* SiO_2 encapsulation of Ag NPs was engineered in an enclosed FSP reactor, as originally described by Sotiriou et al.[43,52] In our study, the desired SiO_2 shell thickness was adjusted in the range of 1 to 5 nm, as detailed in our recent work.[47] Specifically, the flame was enclosed by a metallic tube (9 cm diameter and 20 cm height) to prolong the high temperature residence time and thus control the particle size and crystallinity. A toroidal ring, equipped with 16 equidistant

https://doi.org/10.1021/acs.jpcc.2c07837
J. Phys. Chem. C 2023, 127, 2045−2057

holes, 500 μm diameter, was placed above the metallic tube and used to radially spray the SiO_2 precursor vapor on the Ag particles. 0.5−3 L min^{-1} N_2 was used as a carrier gas (Linde, purity >99%) bubbled through hexamethyldisiloxane (HMDSO, Aldrich, purity 98%), fixed at 10 °C. The N_2-HMDSO stream was injected into the particle field, along with an additional N_2 stream used to enforce the radial convection of the HMDSO vapor, according to the methodology developed by Teleki et al.[53,54] In addition, co-agglomerated Ag/SiO_2 materials were prepared in a single-nozzle FSP reactor by spraying a mixture of silver acetate/HMDSO. The FSP settings and characteristics of the $Ag@SiO_2$ materials are listed in Table S1.

2.3. Sample Preparation for EPR Measurements. Potassium dichromate ($K_2Cr_2O_7$, purity >99%) and oxalic acid ($C_2H_2O_4$, purity >98%) were purchased from Sigma-Aldrich. Stock Cr-oxalate solutions were prepared in degassed ultrapure Milli-Q water (Millipore) at pH = 3, using 10 mM $K_2Cr_2O_7$ and 40 mM $C_2H_2O_4$, purchased from Sigma-Aldrich. At fixed stoichiometry Cr/Oxalate = 1:2, stable [Cr-{oxalate}] complexes are formed, as verified by EPR spectroscopy. Exhaustive degassing of each sample was performed to remove ambient O_2 using a Leybold vacuum pump (10^{-5} bar). For each experiment, fresh Cr-oxalate was used. Every sample was prepared by adding the appropriate amount from the stock Cr-oxalate solution to a freshly prepared suspension of $Ag^0@SiO_2$ in dark conditions. Before irradiation, the system was allowed to equilibrate under mild stirring at room temperature for 15 min. Degassing was an important step to remove ambient O_2 that, otherwise, might act as an adventitious electron acceptor in this type of experiment.

2.4. Irradiation Setup. Irradiation of the samples was performed using an arc xenon lamp (Oriel 6293) operating at 450 W (Figure S1). The power intensity was kept constant and photon-power was recorded at 150 mW cm^{-2} using a power meter (Newport). To eliminate heating effects by the IR photons, a water filter was inserted before the focusing lens. The particle suspensions were irradiated *via* a 90°-reflector mirror holder (model: 62245).

2.5. Monitoring ΔT Variations. The temperature was recorded by an infrared thermal imager (Fluke, TiS40). Considering the SiO_2 surface, the emissivity was set at 0.7 and the background temperature at 22 °C. The standard error values shown at temperature curves are obtained according to the thermal camera's range (±1 °C). Constant stirring during the experiment downgrades the existence of thermal gradients in the surrounding medium.

2.6. Near-Field Simulations. The simulation of electromagnetic hot spots in $Ag@SiO_2$ particle proximity was conducted using MATLAB work package MNPBEM based on the boundary element method (BEM), developed by Garcia de Abajo and Howie.[55] The surrounding medium was water (n = 1.33), and the optical constants of silver were taken by Palik.[56]

2.7. Electron Paramagnetic Resonance. The X-band electron paramagnetic resonance (EPR) spectra were recorded with a Bruker ER200D spectrometer at liquid nitrogen temperature (77 K), equipped with an Agilent 5310A frequency counter. The spectrometer was running under custom-made software based on LabView.[57] Adequate signal-to-noise ratio was obtained after 10 scans, with a microwave power fixed at 8 mW. The EPR instrumental conditions were as follows: microwave frequency 9.54 GHz, modulation frequency = +50.00 kHz, and modulation amplitude = 10 gauss peak-to-peak.

2.8. Cr Mass-Balance Monitoring. The mass balance of the Cr species was monitored according to relation 3. Cr^{6+} was quantified by the well-established diphenylcarbazide (DPC) method using UV−vis spectroscopy,[58] and Cr^{5+}/Cr^{3+} species were quantified using EPR spectroscopy.

2.9. Validation of the Methodology. The present methodology for quantitative monitoring of the hot electrons transferred to the Cr-acceptors requires diligent control of eventual side reactions, as follows: the direct photochemical reduction of the Cr^{6+} ions, has been estimated in control experiments by irradiating the {Cr^{6+}-oxalate} solution, in the absence of $Ag@SiO_2$ nanoparticles. In our irradiation setup, in the absence of NPs, a maximum of ∼10% Cr^{6+} was reduced by direct photolysis, in accordance with Testa et al. (see Figure S15).[37] Cr^{6+}, due to the highly oxidizing potential [E_0 = +1.33 V for the redox couple $Cr^{6+}(ox)_2/Cr^{3+}(ox)_2$], is a very efficient electron acceptor, which renders it a strongly oxidizing agent. Thus, direct Ag-oxidation might lead to Cr^{6+} reduction without the intervention of light, forming Ag ions released in the aqueous solution. Sotiriou et al. have investigated in detail the redox stability of flame-made SiO_2-coated Ag nanoparticles and demonstrated that SiO_2 encapsulation can eliminate the Ag^+ leaching in aqueous suspensions.[49] Therein, the release of Ag^+ ions by an $Ag@SiO_2$/{Cr-oxalate} suspension was found to account for ∼13% of total Cr-reduction, for the 1 nm SiO_2 shell, see Figure S10. As a reference, in co-agglomerated $Ag/50SiO_2$ where Ag is not coated, Cr^{6+} ions were able to oxidize ∼30% of the Ag, amplifying the superior stability of the core@shell structure studied in this work. Furthermore, considering the case of, for example, 0.08 g L^{-1} $Ag@1SiO_2$ (Figure 2), the decrease of Cr^{6+} concentration by ∼1.6 mM cannot be assigned to 0.7 mM Ag in the solution since post-catalysis XPS measurements show no oxidized species at all. Hence Ag^+ release cannot be the prevailing mechanism of Cr^{6+} reduction. The Cr species related to the oxidation mechanism have been subtracted from the total yield.

2.10. $Ag@SiO_2$ Characterization. The morphology and phase composition of the [$Ag@SiO_2$−Cr] system were studied using a scanning electron microscope (SEM, Quanta Inspect, FEI, Eindhoven, Netherlands) coupled with energy-dispersive X-ray spectroscopy (EDS/EDX/EDAX; EDX DX4, Mahwah, NJ, USA) and a FEI Talos F200i field-emission (scanning) transmission electron microscope (Thermo Fisher Scientific Inc., Waltham, MA, USA) operating at 200 kV, equipped with a windowless energy-dispersive spectroscopy microanalyzer (6T/100 Bruker, Hamburg, Germany). XRD data were acquired at room temperature using a Bruker D8 Advance 2theta diffractometer with copper radiation (Cu Kα, λ = 1.5406 Å) and a secondary monochromator operating (40 kV, 40 mA), whereby samples were measured between 10 and 80° (Figure S6). Crystal size is calculated by using the Scherrer formula. UV−vis spectra were collected by a PerkinElmer Lambda 35 spectrometer by dispersing particles in aqueous solvents and placing them in quartz cuvettes. XPS spectra were acquired in a surface analysis ultrahigh vacuum system (SPECS GmbH) equipped with a twin Al−Mg anode X-ray source and a multi-channel hemispherical sector electron analyzer (HSAPhoibos 100). The base pressure was 1−3 × 10^{-9} mbar. A monochromatized Mg Kα line at 1253.6 eV and an analyzer pass energy of 15 eV were used in all XPS measurements. The binding energies were calculated regarding

https://doi.org/10.1021/acs.jpcc.2c07837
J. Phys. Chem. C 2023, 127, 2045−2057

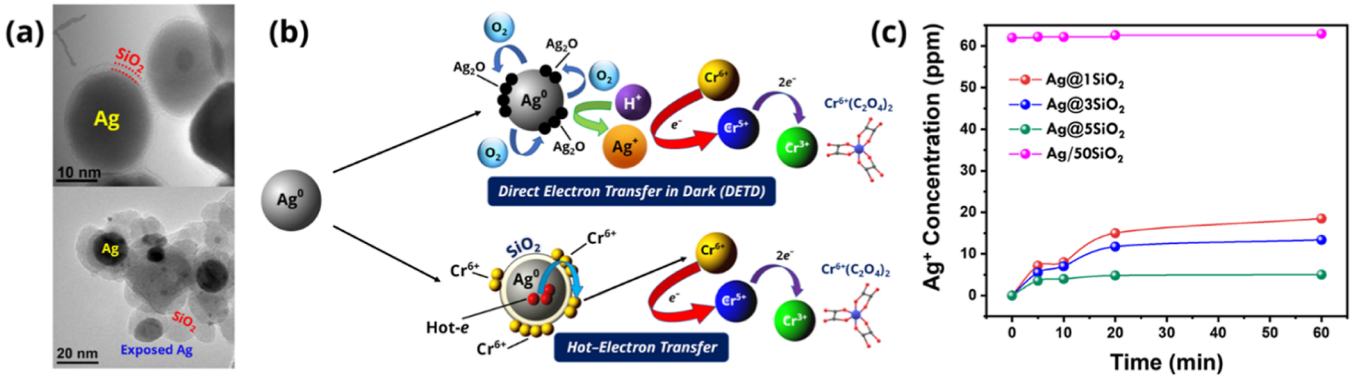

Figure 1. (a) TEM images of core−shell Ag@SiO_2 coated with a 1 nm SiO_2 shell (upper) and Ag particles deposited on SiO_2 with exposed areas (lower). (b) Schematic illustration of possible Cr^{6+} reduction paths: [i] direct reduction of Cr^{6+} *via* oxidation of the non-coated Ag results in the release of oxidized Ag^+ ions under dark conditions and [ii] plasmon-induced hot-electron transfer from plasmonic Ag@SiO_2, where the oxidative path is suppressed. (c) Evolution of Ag^+ release by bare/non-coated Ag or SiO_2-coated Ag (0.5 g L^{-1}). The ultrathin 1 nm SiO_2 shell hinders the contribution of oxidative Ag^+ release to Cr^{6+} reduction by 13%.

the binding energy (BE) of C 1s peak of adventitious carbon at 284.8 eV. The peak deconvolution was calculated using a Shirley background.

2.11. Quantitative EPR. $Cu^{2+}(NO_3)_2$ (S = 1/2) and {Fe^{3+}-EDTA} (S = 5/2) in ethanol, were used as spin standards for the quantitation of the Cr-species according to the quantitation method of Chasteen.[46] Specifically, Cu^{2+} (S = 1/2) is appropriate for quantitation of the Cr^{5+} (S = 1/2) since both have similar spin-relaxation profiles, and $g \sim 2$. On the other hand, {Cr^{3+}-oxalate} and {Fe^{3+}-EDTA} both have broad EPR spectra extending in the same region of magnetic fields, from $g \sim 4$ to $g \sim 2$, thus {Fe^{3+}-EDTA} (S = 5/2) provides a reliable spin-standard for EPR quantitation of high-spin Cr^{3+} (S = 3/2) species. It is underlined that the EPR microwave−saturation profile of the spin systems was measured, and spin quantification was done under non-saturating conditions. In the experimental EPR spectra of the samples irradiated at various times, containing a mixture of Cr^{5+} and Cr^{3+} species, the quantitative analysis of Cr^{5+} and Cr^{3+} consisted of two steps:

i deconvolution of the total experimental EPR spectrum to the Cr^{5+} and Cr^{3+} EPR sub-spectra. This was done by computer simulation of the Cr^{5+}- and Cr^{3+}-EPR signals, as exemplified in Figure 1.

ii then, the double integral of the simulated Cr^{5+} and Cr^{3+} EPR spectra was used to estimate the spin concentration, by comparison with the Cu^{2+} (S = 1/2) and Fe^{3+} (S = 5/2) calibration, respectively.

2.12. EPR Simulation. To simulate the EPR spectrum of Cr^{5+} (S = 1/2) spin system we have used a Zeeman spin-Hamiltonian

$$H = \beta B \cdot \tilde{g} \cdot S \tag{3}$$

where $\tilde{g}$ is the g-tensor and S = 1/2.

The Cr^{3+} (S = 3/2) spin system was simulated using the Spin−Hamiltonian relation 4

$$H = \beta B \cdot \tilde{g} \cdot S + S \cdot \tilde{D} S.$$

$$= \frac{\mu_B}{h}(\vec{B} \cdot g \cdot \vec{S}) + D\left(S_z^2 - \frac{1}{3}S(S+1)\right) + E(S_x^2 - S_y^2) \tag{4}$$

with S = 3/2. The values of the components of the zero-field splitting tensor $\tilde{D}$ (D and E) are related to the electronic configuration symmetry and spin-ligand interaction strength. Specific attention is required when using the S = 5/2 system of Fe^{3+} to quantify the S = 3/2 system of Cr^{3+}, as detailed by Eaton et al.[41] The equation that describes the double integral (DI) of an experimental EPR spectrum and how it relates to the number of spins in the sample is given by

$$\mathrm{DI} = c[G_R C_t n]\left(\frac{\sqrt{P} B_m Q n_B S(S+1) n_S}{f(B_1, B_m)}\right) \propto S(S+1) \tag{5}$$

where c is a constant input to the software from a sample with a known number of spins, G_R the receiver gain, C_t the conversion time, n is the number of scans, P the microwave power in W, B_m the modulation amplitude in gauss, Q is the quality factor of the resonator, n_B the Boltzmann factor for temperature dependence, S and n_S are the total electron spin and the number of spins, respectively, and $f(B_1, B_m)$ is the spatial distribution of the microwave field and the modulation field experienced by the sample.

Thus, when we use the Fe^{3+} (S = 5/2) spins to quantify the Cr^{3+} (S = 3/2) system, a spin-dependent correction factor is applied, see eq 6.

$$\frac{\mathrm{DI}(Cr^{3+}: S_1 = 3/2)}{\mathrm{DI}(Fe^{3+}: S_2 = 5/2)} \sim \frac{S_1(S_1+1)}{S_2(S_2+1)} = \frac{3}{7} \tag{6}$$

where DI is the double integrated area of an EPR signal, recorded under non-saturating microwave power. Finally, attention should be paid to the fact that to convert the amount of Cr^{3+} to the number of electrons, a factor of (×3) must be used since $Cr^{6+} \rightarrow Cr^{3+}$ reduction is a 3-electron event.

Overall, a precise quantitative assessment of the hot-electron transfer to Cr^{6+} can be done based on the control of the mass balance of all Cr species, as described in the mass-balance relation 7

$$[\mathrm{Cr}]_{\mathrm{TOTAL}} = [Cr^{6+}] + [Cr^{5+}] + [Cr^{3+}] \tag{7}$$

Cr^{6+} was quantified by UV−vis spectroscopy, while Cr^{5+} and Cr^{3+} were quantified by EPR.

3. RESULTS AND DISCUSSION

3.1. Ag@SiO_2 Characterization. Table S1 summarizes the structural characteristics of the Ag@SiO_2 particles used in the

https://doi.org/10.1021/acs.jpcc.2c07837
J. Phys. Chem. C 2023, 127, 2045−2057

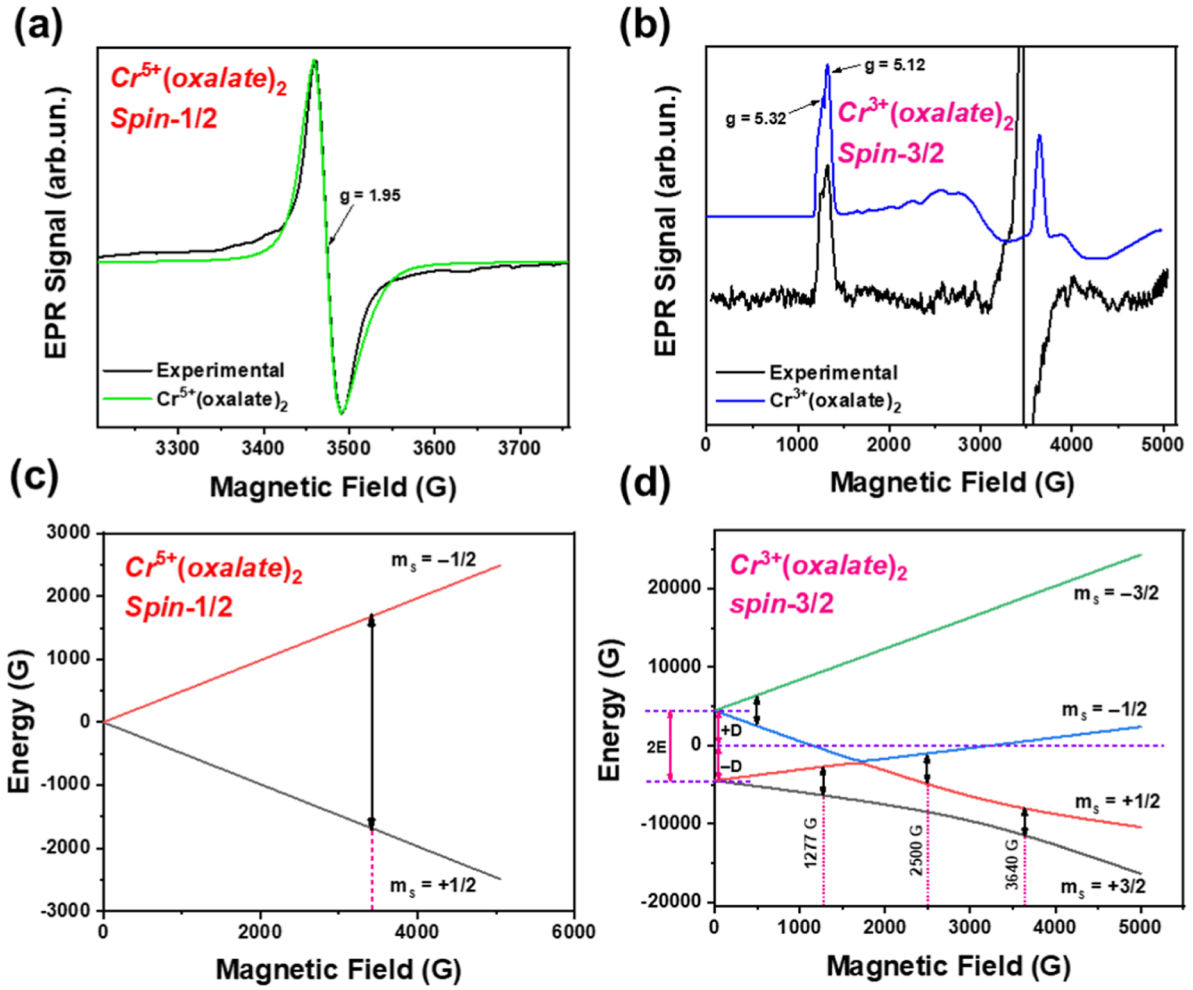

Figure 2. Experimental and simulated EPR signals of (a) $Cr^{5+}(oxalate)_2$ species of spin system $S = 1/2$ and (b) $Cr^{3+}(oxalate)_2$ species of spin system $S = 3/2$, displaying the characteristic axial g-components, that is, $g \sim 2$ and $g \sim 5$, respectively. The detailed spin Hamiltonian parameters are listed in Table 1. These graphs refer to 500 mg L^{-1} $Ag@SiO_2$ NP concentration. (c,d) Calculated energy levels for the $Cr^{5+}(oxalate)_2$ and $Cr^{3+}(oxalate)_2$ species, displaying the possible EPR resonances for the given X band (B_0 = 3400 gauss), obeying the selection rule for transitions $\Delta m_s = \pm 1$. These resonances verify the observed EPR signals of $Cr^{5+}(oxalate)_2$ and $Cr^{3+}(oxalate)_2$ species. For the $Cr^{3+}(oxalate)_2$ system, the Euler angles (orientations) of the magnetic field were equivalent to $[\varphi, \theta] = [\pi/15, 0]$ relative to the molecular frame of the spin system ($S = 3/2$).

present study. TEM and XRD data are presented in Figures S4−S6. For convenience, Figure 1a shows the $Ag@1SiO_2$ particles (upper image) and the Ag particles deposited on SiO_2 (lower image). In all materials, the Ag^0 core diameter was ∼15 nm, while the SiO_2 layer thickness was adjusted in the range of 1−5 nm, as established by other FSP-based studies.[43,47] The SiO_2 shell thickness controls the interparticle distance, as evidenced in the UV/Vis profile (Figure S8), with the resonance at 590 nm assigned to coupled plasmonic particles.[59] XPS study certifies the absence of oxidized Ag species, thus SiO_2 shell acts as an aggregation tuner and a particle protector as well (Figure S7).[60]

3.2. Plasmon-Mediated Hot Carriers versus Direct Electron Transfer in Dark: Evaluation of Ag^+ Leaching. Before starting to consider plasmon-driven phenomena in Cr^{6+} reduction, other mechanisms should be elucidated in the presence of $Ag@SiO_2$. Besides thermal effects, Figure 1b depicts the two possible mechanisms that contribute to Cr^{6+} reduction, the hot electrons and the direct Ag-oxidation by Cr^{6+} under dark conditions. Oxidation of Ag particles occurs in the case of non-coated, exposed Ag surfaces.[61] This oxidative step results in the release of the Ag^+ ions in aqueous solutions, thus monitoring them provides a quantitative measure of the eventual core oxidation. Thus, the SiO_2 coating provides an efficient shield, suppressing Ag^+ release. Under the ultrathin SiO_2 coating ∼1−5 nm, some Ag surfaces can be exposed to Cr^{6+}. This Cr^{6+} reduction *via* the "dark/oxidative" path, is not related to hot-electron transfer, thus it has to be properly accounted for. Herein, to take this into account we have carried out a diligent control of the Ag^+ release, depicted in Figure 1c. The thinner 1 nm SiO_2 layer permits 15 ppm Ag^+ leaching in the first 60 min. Regarding the Cr^{6+} reduction kinetics shown hereafter, this release accounts for 13% of reduced Cr^{6+}, indicating a small portion of bare Ag surface in the $Ag@1SiO_2$. For reference, the Ag^+ leaching of the non-coated Ag/SiO_2 particles reaches 56%, in the same time-interval, as expected for the exposed Ag particles.[59] Hereafter, taking these data into account, we show that the observed photoinduced Cr^{6+} reduction by core@shell $Ag@SiO_2$ originates from plasmon-induced hot electrons, while direct Cr^{6+} reduction *via* Ag-oxidation without illumination is marginal.

3.3. Quantitative Monitoring of Hot-Electron Transfer to {Cr-Oxalate} Species by EPR Spectra. According to

https://doi.org/10.1021/acs.jpcc.2c07837
J. Phys. Chem. C 2023, 127, 2045−2057

Table 1. Spin Hamiltonian Parameters for the {Cr^{3+}-Oxalate} and {Cr^{5+}-Oxalate} Species

{Cr^{5+}-oxalate} species (S = 1/2)			{Cr^{3+}-oxalate} species (S = 3/2)					
$g_x \pm 0.002$	$g_y \pm 0.002$	$g_z \pm 0.002$	$g_x \pm 0.002$	$g_y \pm 0.002$	$g_z \pm 0.002$	D (cm^{-1}) $\pm$ 0.001	E (cm^{-1}) $\pm$ 0.001	$E/D \pm 0.001$
1.965	1.957	1.920	1.915	1.925	1.910	0.417	0.038	0.258

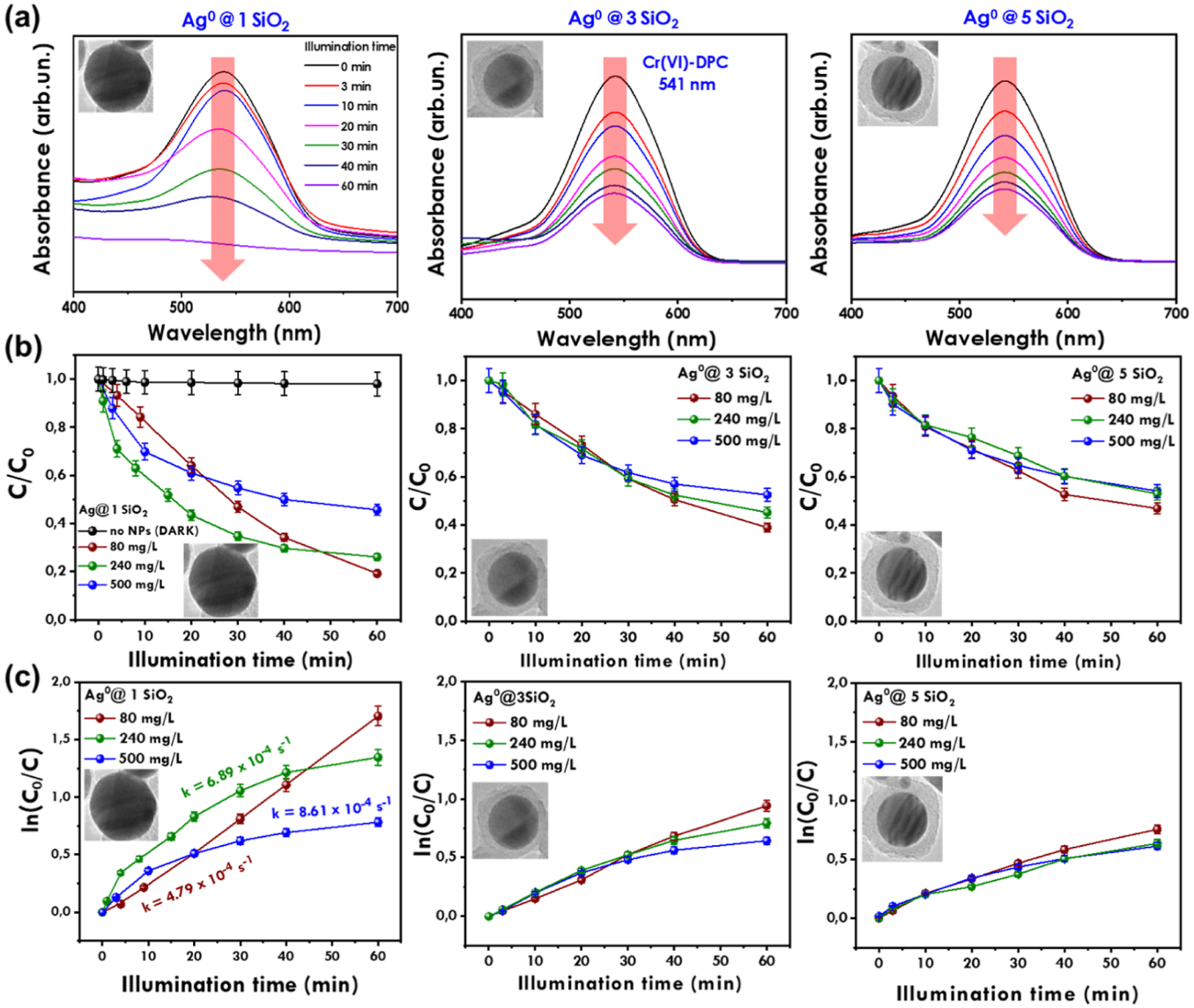

Figure 3. Monitoring of Cr^{6+} photo-reduction by $Ag@SiO_2$ nanoparticles of shell thicknesses of 1, 3, and 5 nm. The SiO_2 shell can be seen in the inset TEM images. (a) UV−vis monitoring of Cr^{6+} reduction by photoinduced hot electrons using $Ag@1SiO_2$, $Ag@3SiO_2$, and $Ag@5SiO_2$, respectively. (b) Kinetics of Cr^{6+} reduction at varying $Ag@SiO_2$ concentrations. The C/C_0 values refer to absorbance at 541 nm normalized to its intensity before irradiation (C_0). (c) [$\ln(C_0/C)$] vs [illumination time] plot. *Insets*: TEM images of $Ag@SiO_2$ NPs for varying SiO_2 shell thickness.

reaction 2, upon irradiation, hot electrons are stimulated, generating {Cr^{5+}-oxalate} and {Cr^{3+}-oxalate} by a sequential one- and two-electron transfer. In this methodology, the EPR fingerprints of {Cr^{5+}-oxalate} and {Cr^{3+}-oxalate} species are identified by the distinct EPR signals, shown in Figure 2. The {Cr^{3+}-oxalate}, that is $[Cr(C_2O_4)_3]^{3-}$ can be easily identified by the characteristic axial g-components in the $g \sim 5$ region, see theoretical spectrum in Figure 2b (blue trace). Similarly, {Cr^{5+}-oxalate} can be identified by the sharp EPR signal at $g \sim 1.9$ in Figure 2a (green trace). In Figure 2b, the total experimental EPR signal (black) contains both {Cr-oxalate} species, as evidenced by the sharp feature at ∼1200 G and the derivative at ∼3500 G. The detailed spin Hamiltonian parameters of {Cr^{5+}/Cr^{3+}-oxalate} species are listed in Table 1.

We underline that the EPR spectrum of Cr^{3+} in Figure 2b corresponds to monomeric *bis*-oxalate Cr^{3+}, that is, {Cr^{3+}-$(oxalate)_2$}$[H_2O]_2$ complex with a distinct EPR fingerprint.[62] In brief, the zero-field splitting D = 0.417 cm^{-1}, estimated by the numerical simulation of the EPR spectrum of {Cr^{3+}-$(oxalate)_2$}, is in very good agreement with the literature for this type of complexes.[39] This D-component gives rise to characteristic effective g-values near $g \sim 5.2-5.4$, which are higher than the typically observed $g \sim 4$ values. Control experiments, in the absence of Ag particles or light, show the

https://doi.org/10.1021/acs.jpcc.2c07837
J. Phys. Chem. C 2023, 127, 2045−2057

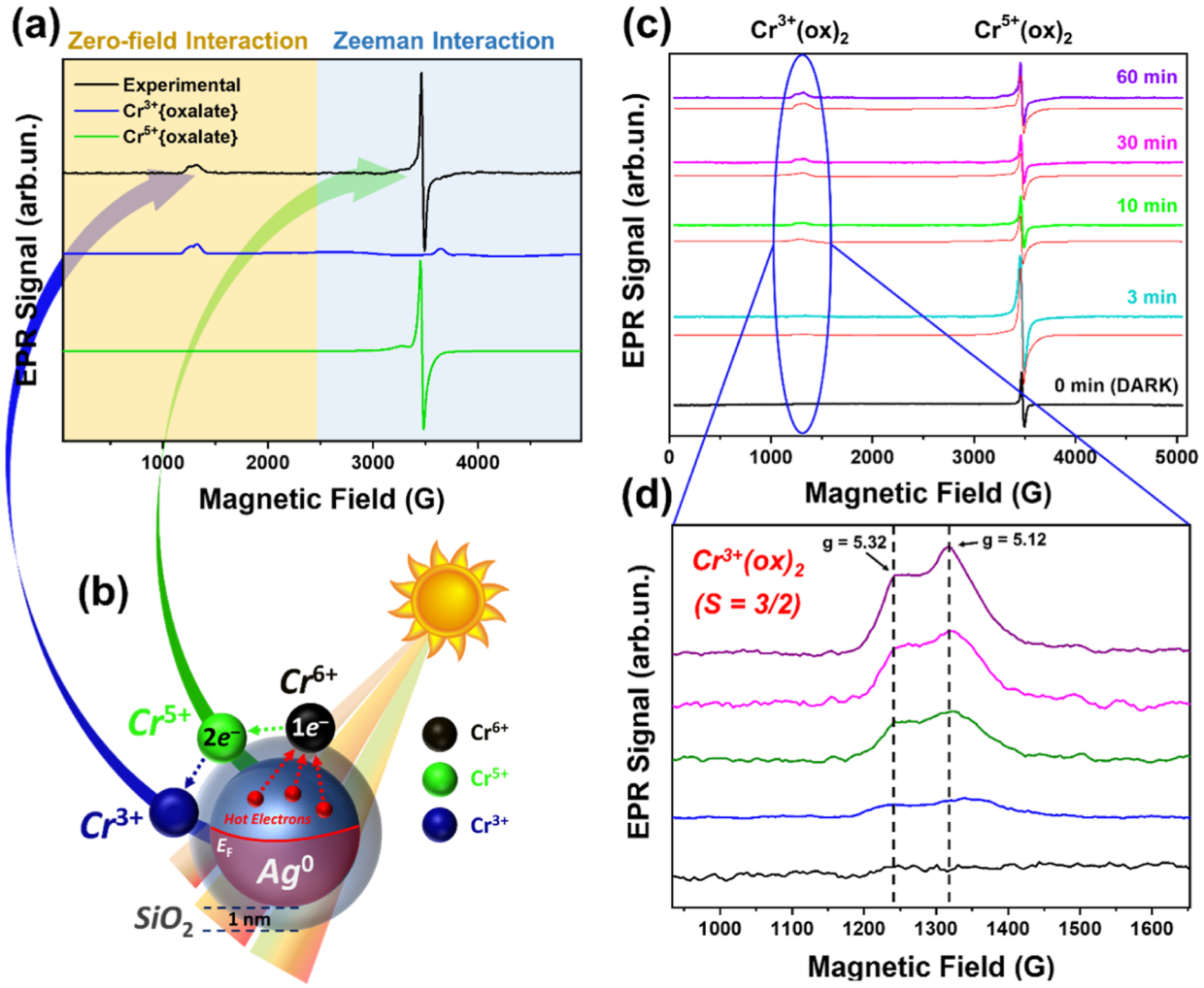

Figure 4. EPR spectra of {Cr^{5+}-oxalate} and {Cr^{3+}-oxalate} species formed via the hot electron-driven reduction of Cr^{6+}. (a) Experimental and simulated EPR signals of Ag@1SiO_2. The EPR spectra for the {Cr^{5+}- and Cr^{3+}-oxalate} species simulations are shown separately for clarity. The spin Hamiltonian parameters used are listed in Table 1. (b) Schematic representing the plasmon-induced Cr^{6+} reduction by the generated hot electrons. The arrows point to promoted reductions, respectively. (c) EPR experimental (colored lines) and simulated (red lines) spectra of {Cr^{5+}-oxalate} and {Cr^{3+}-oxalate} with various times of illumination of Ag@1SiO_2 NPs of concentration 500 mg L^{-1} NP. (d) Magnified Cr^{3+} EPR region is presented, revealing the axial g-tensor of the {Cr^{3+}-oxalate} species. In the absence of irradiation, all these EPR signals were absent.

absence of any EPR signal. Thus, the EPR spectra display the Ag^0@SiO_2/Cr-oxalate system, which produces monomeric {Cr^{5+}-oxalate} and {Cr^{3+}-oxalate} complexes according to the plasmon-driven electron-transfer reaction 2. The formation of monomeric species is underlined since it allows more precise quantitation of the detected Cr-species, thus the hot-electron population according to relation 8

$$N_{\text{hot-e}} = 1 \times [Cr^{5+}] + 3 \times [Cr^{3+}] \quad (8)$$

where $N_{\text{hot-e}}$ is the concentration of hot electrons transferred to {Cr-oxalate} acceptors, and $[Cr^{5+}]$ and $[Cr^{3+}]$ are the concentrations of the Cr-species in μmoles L^{-1}, determined by EPR. For completeness, the non-recombined holes in the photoexcited Ag^0@SiO_2 system were also detected by monitoring the formation of OH radicals using spin-trapping EPR (shown in Figure S13).

3.4. Monitoring Hot-Electron Transfer to Cr^{6+}/Cr^{5+}/Cr^{3+}. An independent route to confirm the injection of hot electrons is to monitor the population of Cr^{6+} species using the well-established diphenylcarbazide (DPC) method.[58] Figure 3a,b presents the kinetics of the Cr^{6+} photo-reduction in the presence of Ag@SiO_2 NPs. The Ag@SiO_2 NP concentration affects drastically the reduction rate. Specifically, at low concentrations (80 mg L^{-1}), at least 80% of Cr^{6+} was photo-reduced within $t \sim 60$ min, while at 500 mg L^{-1} the fastest kinetic rate of Cr^{6+} reduction was observed. Further analysis of the kinetic profile of Cr^{6+} reduction in Figure 3c, reveals that, upon increasing NP concentration, the reaction pathway changes. At 80 mg L^{-1} the quasi−linear profile indicates that the Cr^{6+} photoreduction is a first-order reaction, which concurs with a one-electron transfer process that is as described by reaction 1a. Interestingly, increasing the particle concentration leads to apparent parabolic kinetics of Cr^{6+} reduction, indicating that second-order effects occur as well (Cr^{3+} formation). This can be attributed to the enhanced plasmonic coupling of neighboring NPs that can increase the number of hot electrons and trigger the subsequent two-electron transfer (reaction 1b). The concentrations of 240 and 500 mg L^{-1} in Figure 3c can be fitted by a pseudo-first-order reaction expression, indicating that multi-electron transfer takes place (see reaction 2). Considering the photocatalytic rates per SiO_2 shell thickness and particle concentration, the enhanced

https://doi.org/10.1021/acs.jpcc.2c07837
J. Phys. Chem. C 2023, 127, 2045−2057

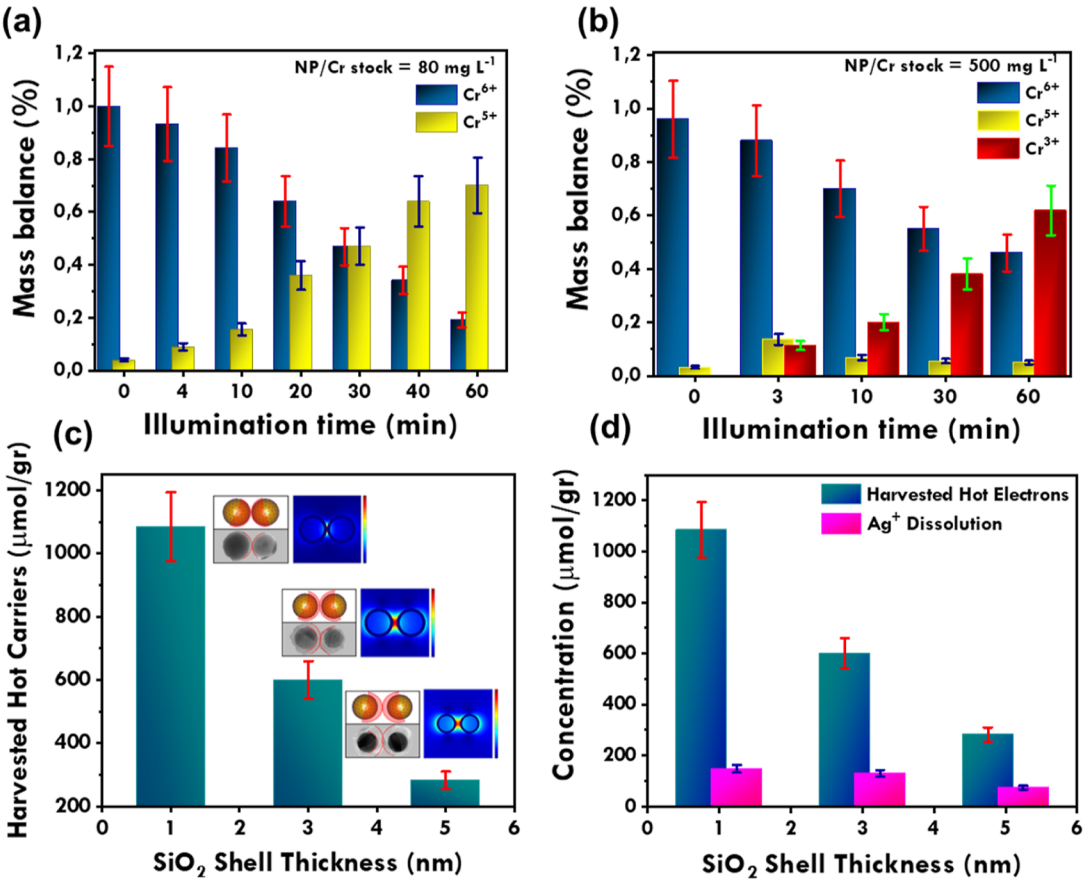

Figure 5. Mass balance (%) of Cr-species and hot electrons. (a) Low Ag@1SiO$_2$ concentration, 80 mg L^{-1}. (b) High Ag@1SiO$_2$ concentration of 500 mg L^{-1}. In both graphs, as Cr^{6+} is reduced, Cr^{5+} or/and Cr^{3+} increase. (c) Quantitation of hot electrons and the apparent quantum yield vs the thickness of SiO$_2$ coating in 500 mg L^{-1}Ag@SiO$_2$ after 10 min of illumination. *Insets*: schematic figures of NP−NP vicinity and TEM images. The calculated near-field mapping profile of each NP configuration. (d) Ag^+ leaching concentrations measured under dark conditions remain far below the amounts of Cr^{5+}/Cr^{3+}-oxalates and thus the harvested hot electrons.

plasmonic coupling of 500 mg L^{-1} Ag@1SiO$_2$ promotes the elevated electron transfer and yields superior performance; therefore, this case will be further studied. It is underlined that three types of control experiments were carried out: [i] in the absence of Ag@SiO$_2$ under dark conditions, no Cr-reduction was observed at all. [ii] negligible presence that is ∼3.5% of {Cr^{5+}-oxalate} was obtained during the 10 min mixing of Ag@1SiO$_2$ NPs and Cr^{6+} in the dark. This is a marginal Cr-reduction via Ag-oxidation in the dark that correlates to Ag^+ leaching as shown in Figure 1c, where 14 ppm in the first 10 min accounts for ∼3% reduced Cr^{6+}. Hence, the contribution of Ag-oxidation in the total reaction is diminished compared to the plasmon-driven phenomena. [iii] Under UV/Vis irradiation without particles, ∼10% of the {Cr-oxalate} was reduced due to direct photolysis that is well known to occur by <300 nm UV-photons.[63] In our analysis, this fraction has been deducted from the total yield. Under visible-light photons $\lambda >$ 340 nm, the photolysis of {Cr-oxalate} was almost zero (Figure S15 in Supporting Information), thus the dominant contribution to the observed Cr reduction is the plasmon-induced electron transfer.

3.5. Quantitative Analysis of Hot-Electron Transfer. Figure 4a,b presents the kinetics of the EPR spectra for the {Cr-oxalate} species formed in the presence of the Ag@1SiO$_2$ NPs under irradiation. In Figure 4c,d, the EPR spectra contained a negligible {Cr^{5+}-oxalate} signal under dark. The Cr mass-balance analysis (eq 3), for low Ag@SiO$_2$ concentration (80 mg L^{-1}) and for high concentration (500 mg L^{-1}), is presented in Figure 5a,b respectively. The correlation confirms that at low particle concentrations, after 60 min of irradiation, ∼80% of the initial Cr^{6+} atoms have been reduced to Cr^{5+}, that is, by a one-electron reduction process. At high particle concentrations, the Cr^{5+} kinetics display a volcano behavior: initially, one-electron acceptor Cr^{5+} species are formed for irradiation times up to ∼3 min at the expense of Cr^{6+}. Then, at prolonged irradiation times up to 60 min, the 3-electron acceptors Cr^{3+}-oxalates are accumulated at the expense of Cr^{5+}, in agreement with previous EPR studies.[37,38] Increased concentration of Ag@1SiO$_2$ promotes the Cr^{3+} formation as more energetic electrons become available plus the increased presence of the local electric fields, in a similar way to the DPC method.

For completeness, the photoinduced hole formation has been monitored by EPR as well (Figure S13 in Supporting Information). The detection of OH radicals confirms that by tuning SiO$_2$-shell thickness, the generation and sufficient separation of hot carriers can be achieved in Ag@SiO$_2$ nanoaggregates.

The population of Cr^{5+} and Cr^{3+} normalized as [μmoles Cr] per [gram of Ag@SiO$_2$] after 10 min of illumination for 500 mg L^{-1} Ag^0@SiO$_2$ is shown in Figure 5c. Regarding shell thickness, a rapid depletion of the hot-electron population is observed by increasing the interparticle distance. The 1 nm shell allows a significant number of energetic electrons to be

https://doi.org/10.1021/acs.jpcc.2c07837
J. Phys. Chem. C 2023, 127, 2045−2057

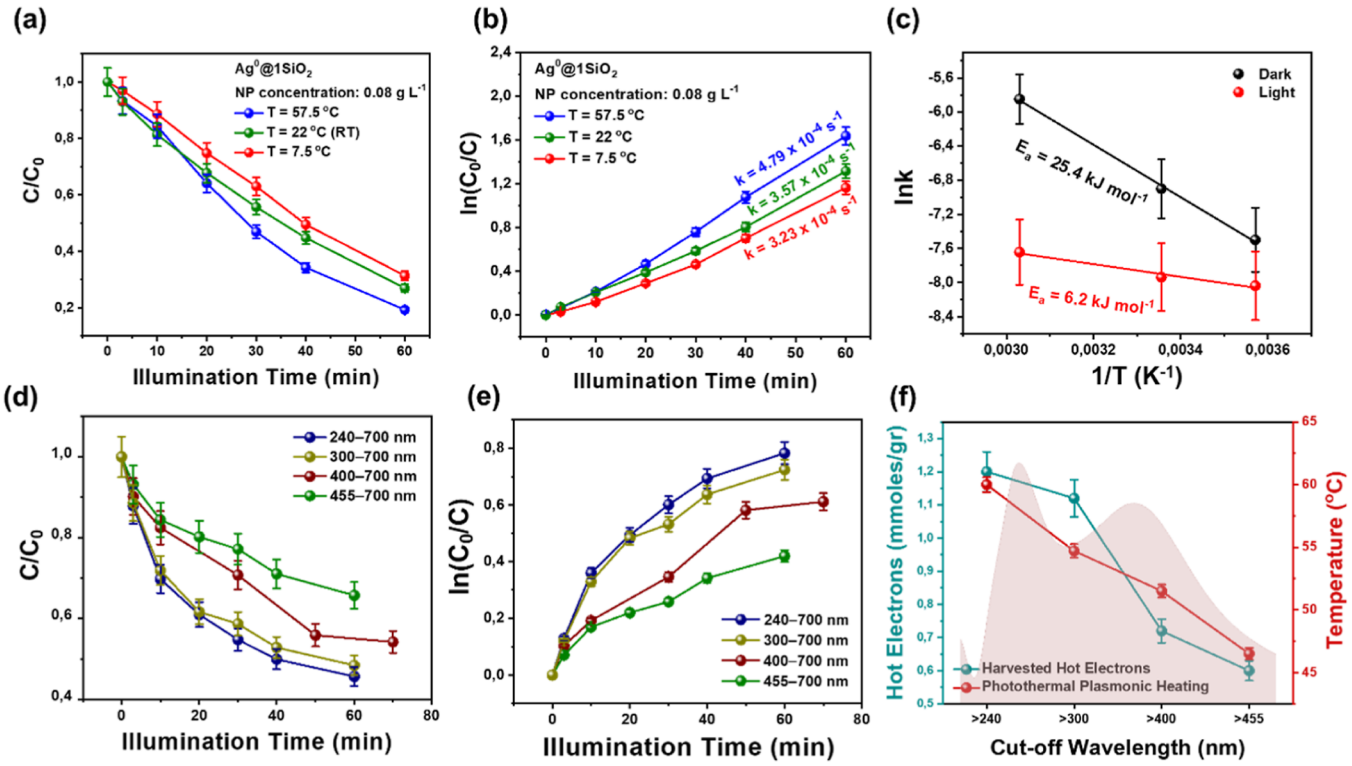

Figure 6. (a–c) Temperature dependence of Cr reduction, by 0.08 g L^{-1} Ag@1SiO_2. (a) Reaction-order graph [ln(C/C_0) vs T] indicates that at all temperatures, the process is first-order. Bulk-temperature change from 7.5 to 57.5 °C has limited effect on the kinetic rates. (b) Kinetics graph for Cr^{6+} reduction by Ag@1SiO_2 NPs for three different solution temperatures (7.5, 22, and 57.5 °C). (c) Arrhenius plot of Ag@1SiO_2/{Cr-oxalate} under dark and light. The activation energies are E_a = 25 kJ mol^{-1} and 6 kJ mol^{-1}, respectively. Under light, the temperature was fixed at the same values measured under dark. (d,e) Effect of the excitation wavelength on Cr^{6+} reduction, using various light long-pass filters (240–700, 300–700, 450–700, and 455–700 nm). (f) Cr^{5+}/Cr^{3+} species (hot electrons) and plasmon-induced bulk temperature using various light cut-off filters. (The UV–vis absorption spectrum of Ag@1SiO_2 is indicated in brown shade.)

transferred, hence the superior performance, correlating in a similar way observed by increasing particle concentration. Again, the contribution of the increased number of hot spots should be noted for the thin-shell case, as they are known for promoting hot carrier generation.[21,25]

3.6. Disentangling the Role of Hot-Electron Transfer and Thermal Effects in the Plasmon-Enhanced Cr-Reduction Mechanism. In our recent work, we have discussed in detail the photothermal effects implicated in the irradiation of Ag^0@SiO_2 NPs.[47] Hereafter, we have further investigated the role of bulk-medium temperature and wavelength irradiation, in the hot-electron transfer efficiency, as shown in Figure 6. Strikingly, the charge-transfer kinetics at T = 7.5, 33, and 57.5 °C show a rather low sensitivity to temperature changes of the bulk medium, thus the estimated first-order reaction rates k, calculated in Figure 6a,b, were in the range 3.2 to 4.8 × 10^{-4} s^{-1}. Figure 6c depicts that the activation energy for illuminated Ag@1SiO_2 was E_a = 6.2 kJ mol^{-1}, which is much lower than the observed E_a = 25.4 kJ mol^{-1} in dark conditions, in the typical range for reactions involving redox-induced electron transfer (20–90 kJ mol^{-1}).[64,65] Recently, Halas' group reported that a substantial light-induced reduction of the activation barrier takes place in plasmon-enhanced photocatalytic processes when hot carriers are involved.[66−68] This corroborates our present findings of decreased activation energy in photocatalytic Cr^{6+} reduction by Ag@SiO_2.

However, the debate that has been emerged by the aforementioned work,[69,70] necessitates the careful measurement of the photothermal effects as well.[71,72] Herein, to further peer into the plasmon-driven mechanism, the role of the excitation wavelength in Ag@1SiO_2 was studied where visible-light filters were employed during the Cr^{6+} photo-reduction, as shown in Figure 6d,e. As expected, cutting off the plasmon resonance at $\lambda \sim 400$ nm resulted in diminished efficiency. Further cutting off the optical region while maintaining the same power intensity (150 mW cm^{-2}), Cr^{6+} reduction was further decreased indicating that photon energy away than the LSPR peak had a lower contribution in the reaction. The profile of thermal effects in Figure 6f shows that by cutting off the plasmon resonance wavelength has a less severe impact on the photothermal performance compared to the reaction yield. Specifically, the steep diminution of the Cr^{5+}/Cr^{3+} species when $\lambda < 400$ nm region was cut-off resembles to electronic transitions, while the linear decrease of photothermal heating tends to follow the absorption spectrum as expected. On a similar note, to the light-induced decreased activation barrier, this observation strengthens the claim that hot-electron transfer is the prevailing mechanism, since the role of thermal effects is minimized.

Overall, based on the above findings, a conceptual energy diagram is proposed in Figure 7a. Hot electrons can be transferred to the external electron acceptor {Cr-oxalate} directly overcoming the barrier posed by the SiO_2 shell. Engineering the shell thickness, the interparticle nanogaps can be tuned by determining the hot-spot intensity and thus the enhanced transfer of these energetic electrons to the {Cr-oxalates}. In this scheme, hot spots are seemingly promoters of

https://doi.org/10.1021/acs.jpcc.2c07837
J. Phys. Chem. C 2023, 127, 2045−2057

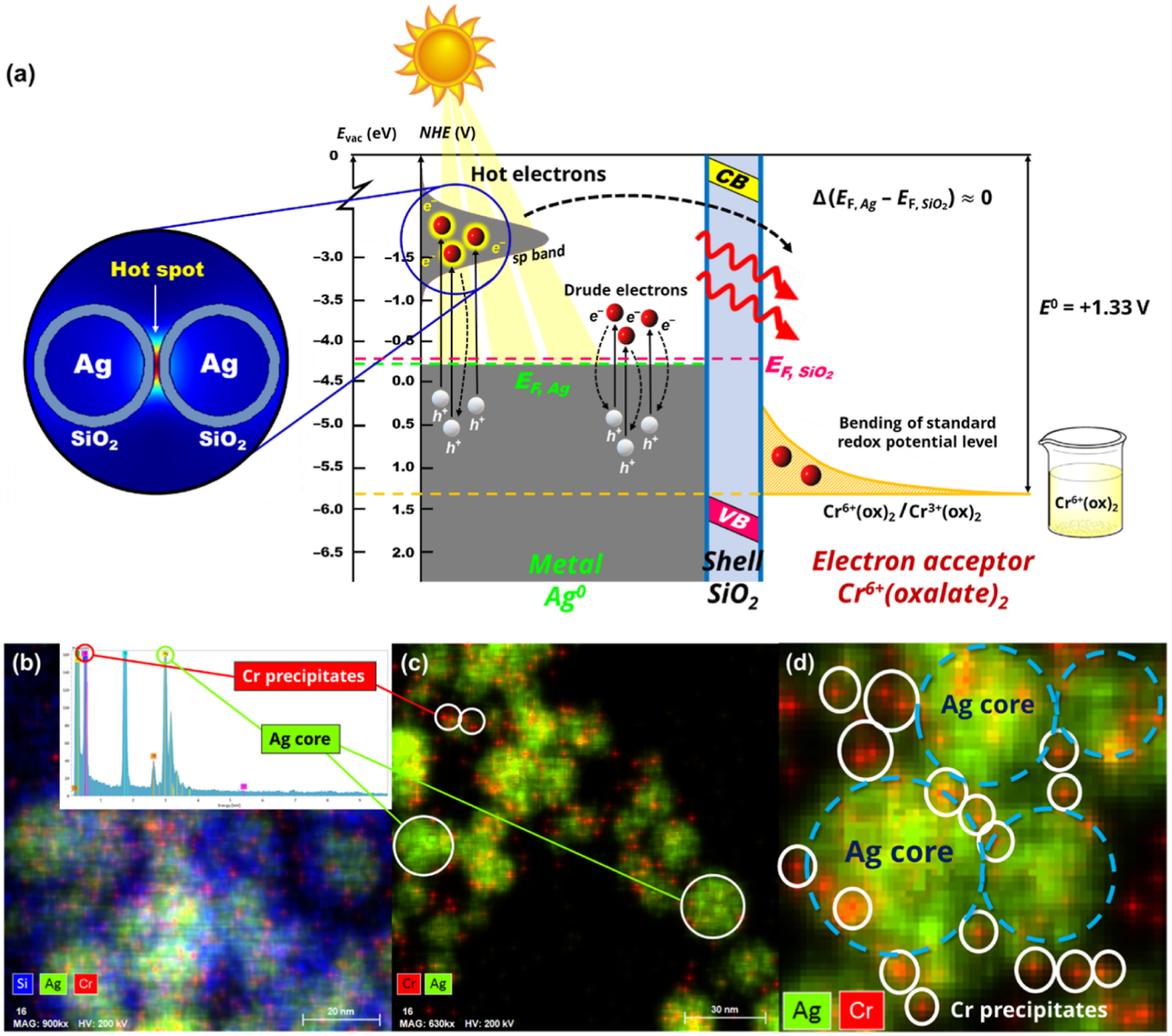

Figure 7. (a) Schematic illustration of the energy diagram of the core@shell−adsorbate [Ag^0@SiO_2/{Cr^{6+}-oxalate}] system, demonstrating the bending of the redox potential level of the adsorbate {$Cr^{6+}(ox)_2/Cr^{3+}(ox)_2$} during illumination. STEM images of Ag@1SiO_2/{Cr-oxalate} system post-illumination, (b) showing Ag, Si, and Cr (in green, blue, and red colors, respectively), (c) Ag and Cr precipitates (in green and red colors), and (d) an indicative magnified region of (c), showing the Cr precipitates (red color, marked in white circles) at the interface of Ag nanoparticles. *Inset:* EDS/EDX spectrum for Ag@1SiO_2 (500 mg L^{-1}) post-photocatalysis. The Ag, Si, and Cr peaks are detected. The Cr precipitates are expected to be $Cr(OH)_3$ during Cr^{6+} reduction.

hot-electron generation, as indicated by the enhanced performance of the 1 nm shell (i.e., the closely coupled particles). STEM images, Figure 7b−d depicts that Cr species are accumulated on the Ag@SiO_2 particles after irradiation. These are attributed to Cr^{3+}species that are known to have a strong tendency to precipitate in aqueous solutions. Probably, the accumulation on the Ag@SiO_2 surface, as seen in STEM, can be higher at the interface of coupled particles where the hot-spots prevail. This is an interesting possibility that deserves further study. In any case, from the environmental-remediation point of view, the present results indicate that the plasmonic Ag@SiO_2 nanoaggregates may play a dual role in Cr^{6+} reduction *via* these highly energetic hot electrons to Cr^{3+} species, plus to attract them on the particle surface.

4. CONCLUSIONS

The efficient photoreduction of hexavalent Cr^{6+} can be achieved by photoexcited Ag@SiO_2 plasmonic nanoaggregates. The present work introduces a novel experimental concept and methodology for trapping and quantitative assessment of plasmon-induced hot electrons generated by core@shell plasmonic nanoaggregates, based on EPR spectroscopy. Cr species are efficient electron acceptors, and progressive one- and three-electron events are mapped via monitoring of the intermediate states Cr^{5+} (S = 1/2) and Cr^{3+} (S = 3/2). Plasmonic coupling is the key parameter for successful transfer of the energetic carriers from the interior of the plasmonic nanocrystal to the exterior/interfacial Cr-acceptor. FSP provides a state-of-the-art technology to control interparticle distance by engineering the shell thickness. The case of an

https://doi.org/10.1021/acs.jpcc.2c07837
J. Phys. Chem. C 2023, 127, 2045−2057

ultrathin SiO_2 shell allows a considerable hot-electron transfer and a light-induced lowering of the activation barrier, while the role of thermal effects and Ag-oxidation phenomena is minimized. The present findings offer a new dimension on plasmon-driven photoreduction of hexavalent Cr^{6+}, in terms of solar-driven environmental remediation.

■ ASSOCIATED CONTENT

Supporting Information

The Supporting Information is available free of charge at https://pubs.acs.org/doi/10.1021/acs.jpcc.2c07837.

Further details on UV/vis analysis of Cr species; details on the Ag^+ leaching experimental procedure; schematic illustration of thr illumination setup; further characterization of $Ag@SiO_2$ particles (TEM images, TEM-derived particle size distribution, and XRD, UV/vis, and XPS spectra); detection of photo-generated OH radicals; and control experiments of particle-free Cr^{6+} reduction (PDF)

■ AUTHOR INFORMATION

Corresponding Author

Yiannis Deligiannakis − *Department of Physics, University of Ioannina (UOI), Ioannina 45110, Greece;* orcid.org/0000-0002-9390-4222; Email: ideligia@uoi.gr

Authors

Constantinos Moularas − *Department of Physics, University of Ioannina (UOI), Ioannina 45110, Greece;* orcid.org/0000-0003-3292-0533

Christos Dimitriou − *Department of Physics, University of Ioannina (UOI), Ioannina 45110, Greece*

Yiannis Georgiou − *Department of Physics, University of Ioannina (UOI), Ioannina 45110, Greece; Foundation for Research and Technology, Hellas−Institute of Chemical Engineering Sciences (FORTH/ICE-HT), Patras 26504, Greece;* orcid.org/0000-0002-9848-9355

Georgios Evangelakis − *Department of Physics, University of Ioannina (UOI), Ioannina 45110, Greece*

Nikos Boukos − *Institute of Nanoscience and Nanotechnology (INN), NCSR Demokritos, Athens 15310, Greece;* orcid.org/0000-0001-7542-0649

Complete contact information is available at: https://pubs.acs.org/10.1021/acs.jpcc.2c07837

Notes

The authors declare no competing financial interest.

■ ACKNOWLEDGMENTS

We acknowledge support of this work by the project "*Center For Research, Quality Analysis Of Cultural Heritage Materials And Communication Of Science*" (MIS 5047233), which is implemented under the Action "Reinforcement of the Research and Innovation Infrastructure", funded by the Operational Programme "Competitiveness, Entrepreneurship, and Innovation" (NSRF 2014−2020) and co-financed by Greece and the European Union (European Regional Development Fund).

■ REFERENCES

(1) Järup, L. Hazards of Heavy Metal Contamination. *British Medical Bulletin* **2003**, *68*, 167−182.

(2) Yang, L.; Xiao, Y.; Liu, S.; Li, Y.; Cai, Q.; Luo, S.; Zeng, G. Photocatalytic Reduction of Cr(VI) on WO_3 Doped Long TiO_2 Nanotube Arrays in the Presence of Citric Acid. *Applied Catalysis B: Environmental* **2010**, *94*, 142−149.

(3) Linic, S.; Christopher, P.; Ingram, D. B. Plasmonic-Metal Nanostructures for Efficient Conversion of Solar to Chemical Energy. *Nat. Mater.* **2011**, *10*, 911−921.

(4) Zhang, Y.; He, S.; Guo, W.; Hu, Y.; Huang, J.; Mulcahy, J. R.; Wei, W. D. Surface-Plasmon-Driven Hot Electron Photochemistry. *Chem. Rev.* **2018**, *118*, 2927−2954.

(5) Christopher, P.; Xin, H.; Linic, S. Visible-Light-Enhanced Catalytic Oxidation Reactions on Plasmonic Silver Nanostructures. *Nature Chem* **2011**, *3*, 467−472.

(6) Cortés, E.; Besteiro, L. V.; Alabastri, A.; Baldi, A.; Tagliabue, G.; Demetriadou, A.; Narang, P. Challenges in Plasmonic Catalysis. *ACS Nano* **2020**, *14*, 16202−16219.

(7) Halas, N. J.; Lal, S.; Chang, W.-S.; Link, S.; Nordlander, P. Plasmons in Strongly Coupled Metallic Nanostructures. *Chem. Rev.* **2011**, *111*, 3913−3961.

(8) Schuller, J. A.; Barnard, E. S.; Cai, W.; Jun, Y. C.; White, J. S.; Brongersma, M. L. Plasmonics for Extreme Light Concentration and Manipulation. *Nat. Mater.* **2010**, *9*, 193−204.

(9) Baffou, G. Q.Thermo-Plasmonics: Using Metallic Nanostructures as Nano-Sources of Heat. *Laser Photonic Rev***2012**, *1−17*. DOI: 10.1002/lpor.201200003

(10) Hartland, G. V. Optical Studies of Dynamics in Noble Metal Nanostructures. *Chem. Rev.* **2011**, *111*, 3858−3887.

(11) Brongersma, M. L.; Halas, N. J.; Nordlander, P. Plasmon-Induced Hot Carrier Science and Technology. *Nat. Nanotechnol.* **2015**, *10*, 25−34.

(12) Hartland, G. V.; Besteiro, L. V.; Johns, P.; Govorov, A. O. What's so Hot about Electrons in Metal Nanoparticles? *ACS Energy Letters* **2017**, *2*, 1641−1653.

(13) Warren, S. C.; Thimsen, E. Plasmonic Solar Water Splitting. *Energy Environ. Sci.* **2012**, *5*, 5133−5146.

(14) Ingram, D. B.; Linic, S. Water Splitting on Composite Plasmonic-Metal/Semiconductor Photoelectrodes: Evidence for Selective Plasmon-Induced Formation of Charge Carriers near the Semiconductor Surface. *J. Am. Chem. Soc.* **2011**, *133*, 5202−5205.

(15) Lee, J.; Mubeen, S.; Ji, X.; Stucky, G. D.; Moskovits, M. Plasmonic Photoanodes for Solar Water Splitting with Visible Light. *Nano Lett.* **2012**, *12*, 5014−5019.

(16) Zhou, L.; Martirez, J. M. P.; Finzel, J.; Zhang, C.; Swearer, D. F.; Tian, S.; Robatjazi, H.; Lou, M.; Dong, L.; Henderson, L.; Christopher, P.; Carter, E. A.; Nordlander, P.; Halas, N. J. Light-Driven Methane Dry Reforming with Single Atomic Site Antenna-Reactor Plasmonic Photocatalysts. *Nat Energy* **2020**, *5*, 61−70.

(17) Hou, W.; Hung, W. H.; Pavaskar, P.; Goeppert, A.; Aykol, M.; Cronin, S. B. Photocatalytic Conversion of CO2 to Hydrocarbon Fuels via Plasmon-Enhanced Absorption and Metallic Interband Transitions. *ACS Catal.* **2011**, *1*, 929−936.

(18) Robatjazi, H.; Bao, J. L.; Zhang, M.; Zhou, L.; Christopher, P.; Carter, E. A.; Nordlander, P.; Halas, N. Plasmon-driven carbon-fluorine (C(sp3)-F) bond activation with mechanistic insights into hot-carrier-mediated pathways. *Nat Catal* **2020**, *3*, 564−573.

(19) Seemala, B.; Therrien, A. J.; Lou, M.; Li, K.; Finzel, J. P.; Qi, J.; Nordlander, P.; Christopher, P. Plasmon-Mediated Catalytic O2 Dissociation on Ag Nanostructures: Hot Electrons or Near Fields? *ACS Energy Lett* **2019**, *4*, 1803−1809.

(20) Manjavacas, A.; Liu, J. G.; Kulkarni, V.; Nordlander, P. Plasmon-Induced Hot Carriers in Metallic Nanoparticles. *ACS Nano* **2014**, *8*, 7630−7638.

(21) Besteiro, L. V.; Govorov, A. O. Amplified Generation of Hot Electrons and Quantum Surface Effects in Nanoparticle Dimers with Plasmonic Hot Spots. *J. of Physical Chemistry C* **2016**, *120*, 19329−19339.

(22) Harutyunyan, H.; Martinson, A. B. F.; Rosenmann, D.; Khorashad, L. K.; Besteiro, L. V.; Govorov, A. O.; Wiederrecht, G. P. Anomalous Ultrafast Dynamics of Hot Plasmonic Electrons in

Nanostructures with Hot Spots. *Nat. Nanotechnol.* **2015**, *10*, 770−774.
(23) Kong, X.-T.; Wang, Z.; Govorov, A. O. Plasmonic Nanostars with Hot Spots for Efficient Generation of Hot Electrons under Solar Illumination. *Advanced Optical Materials* **2017**, *5*, 594.
(24) Santiago, E. Y.; Besteiro, L. V.; Kong, X.-T.; Correa-Duarte, M. A.; Wang, Z.; Govorov, A. O. Efficiency of Hot-Electron Generation in Plasmonic Nanocrystals with Complex Shapes: Surface-Induced Scattering, Hot Spots, and Interband Transitions. *ACS Photonics* **2020**, *7*, 2807−2824.
(25) Besteiro, L. V.; Yu, P.; Wang, Z.; Holleitner, A. W.; Hartland, G. V.; Wiederrecht, G. P.; Govorov, A. O. The Fast and the Furious: Ultrafast Hot Electrons in Plasmonic Metastructures. Size and Structure Matter. *Nano Today* **2019**, *27*, 120−145.
(26) Jang, Y. J.; Chung, K.; Lee, J. S.; Choi, C. H.; Lim, J. W.; Kim, D. H. Plasmonic Hot Carriers Imaging: Promise and Outlook. *ACS Photonics* **2018**, *5*, 4711−4723.
(27) Besteiro, L. V.; Kong, X.-T.; Wang, Z.; Hartland, G.; Govorov, A. O. Understanding Hot-Electron Generation and Plasmon Relaxation in Metal Nanocrystals: Quantum and Classical Mechanisms. *ACS Photonics* **2017**, *4*, 2759−2781.
(28) Lock, D.; Rusimova, K. R.; Pan, T. L.; Palmer, R. E.; Sloan, P. A. Atomically Resolved Real-Space Imaging of Hot Electron Dynamics. *Nat. Commun.* **2015**, *6*, 8365.
(29) Hu, M.; Novo, C.; Funston, A.; Wang, H.; Staleva, H.; Zou, S.; Mulvaney, P.; Xia, Y.; Hartland, G. V. Dark-Field Microscopy Studies of Single Metal Nanoparticles: Understanding the Factors That Influence the Linewidth of the Localized Surface Plasmon Resonance. *J. Mater. Chem.* **2008**, *18*, 1949.
(30) Giugni, A.; Torre, B.; Toma, A.; Francardi, M.; Malerba, M.; Alabastri, A.; Proietti Zaccaria, R.; Stockman, M. I.; Di Fabrizio, E. Hot-Electron Nanoscopy Using Adiabatic Compression of Surface Plasmons. *Nat. Nanotechnol.* **2013**, *8*, 845−852.
(31) Segal, E.; Galanty, M.; Aharon, H.; Salomon, A. Visualization of Plasmon-Induced Hot Electrons by Scanning Electron Microscopy. *The Journal of Physical Chemistry C* **2019**, *123*, 30528−30535.
(32) Reddy, H.; Wang, K.; Kudyshev, Z.; Zhu, L.; Yan, S.; Vezzoli, A.; Higgins, S. J.; Gavini, V.; Boltasseva, A.; Reddy, P.; Shalaev, V. M.; Meyhofer, E. Determining Plasmonic Hot-Carrier Energy Distributions via Single-Molecule Transport Measurements. *Science* **2020**, *369*, 423−426.
(33) Cortés, E.; Xie, W.; Cambiasso, J.; Jermyn, A. S.; Sundararaman, R.; Narang, P.; Schlücker, S.; Maier, S. A. Plasmonic Hot Electron Transport Drives Nano-Localized Chemistry. *Nat. Commun.* **2017**, *8*, 14880.
(34) Simoncelli, S.; Li, Y.; Cortés, E.; Maier, S. A. Nanoscale Control of Molecular Self-Assembly Induced by Plasmonic Hot-Electron Dynamics. *ACS Nano* **2018**, *12*, 2184−2192.
(35) Zhai, Y.; DuChene, J. S.; Wang, Y.-C.; Qiu, J.; Johnston-Peck, A. C.; You, B.; Guo, W.; DiCiaccio, B.; Qian, K.; Zhao, E. W.; Ooi, F.; Hu, D.; Su, D.; Stach, E. A.; Zhu, Z.; Wei, W. D. Polyvinylpyrrolidone-Induced Anisotropic Growth of Gold Nanoprisms in Plasmon-Driven Synthesis. *Nat. Mater.* **2016**, *15*, 889−895.
(36) Yu, Y.; Wijesekara, K. D.; Xi, X.; Willets, K. A. Quantifying Wavelength-Dependent Plasmonic Hot Carrier Energy Distributions at Metal/Semiconductor Interfaces. *ACS Nano* **2019**, *13*, 3629−3637.
(37) Testa, J. J.; Grela, M. A.; Litter, M. I. Heterogeneous Photocatalytic Reduction of Chromium(VI) over TiO_2 Particles in the Presence of Oxalate: Involvement of Cr(V) Species. *Environ. Sci. Technol.* **2004**, *38*, 1589−1594.
(38) Giannakas, A. E.; Seristatidou, E.; Deligiannakis, Y.; Konstantinou, I. Photocatalytic Activity of N-Doped and N−F Co-Doped TiO_2 and Reduction of Chromium(VI) in Aqueous Solution: An EPR Study. *Applied Catalysis B: Environmental* **2013**, *132*−*133*, 460−468.
(39) Pattison, D. I.; Lay, P. A.; Davies, M. J. EPR Studies of Chromium(V) Intermediates Generated via Reduction of Chromium-(VI) by DOPA and Related Catecholamines: Potential Role for Oxidized Amino Acids in Chromium-Induced Cancers. *Inorg. Chem.* **2000**, *39*, 2729−2739.
(40) Farrell, R. P.; Lay, P. A.; Levina, A.; Maxwell, I. A.; Bramley, R.; Brumby, S. An EPR Spectroscopic Study of Chromium(V) Oxalato Complexes in Aqueous Solutions. Mechanism of the Chromium(VI) Oxidation of Oxalic Acid. *Inorg. Chem.* **1998**, *37*, 3159−3166.
(41) Eaton, G. R.; Eaton, S. S.; Barr, D. P.; Weber, R. T.; Wiedeń, S.-V.*Quantitative EPR*; Springer: Wien; New York, 2014.
(42) Deligiannakis, Y.; Louloudi, M.; Hadjiliadis, N. Electron Spin Echo Envelope Modulation (ESEEM) Spectroscopy as a Tool to Investigate the Coordination Environment of Metal Centers. *Coord. Chem. Rev.* **2000**, *204*, 1−112.
(43) Sotiriou, G. A.; Blattmann, C. O.; Deligiannakis, Y. Nano-antioxidant-Driven Plasmon Enhanced Proton-Coupled Electron Transfer. *Nanoscale* **2016**, *8*, 796−803.
(44) Mitrikas, G.; Deligiannakis, Y.; Trapalis, C. C.; Boukos, N.; Kordas, G. CW and Pulsed EPR Study of Silver Nanoparticles in a SiO_2 Matrix. *J. Sol-Gel Sci. Technol.* **1998**, *13*, 503−508.
(45) Moularas, C.; Psathas, P.; Deligiannakis, Y. Electron Paramagnetic Resonance Study of Photo-Induced Hole/Electron Pairs in NaTaO3 Nanoparticles. *Chem. Phys. Lett.* **2021**, *782*, 139031.
(46) Bou-Abdallah, F.; Chasteen, N. D. Spin Concentration Measurements of High-Spin (G′ = 4.3) Rhombic Iron(III) Ions in Biological Samples: Theory and Application. *J. Biol. Inorg Chem.* **2007**, *13*, 15−24.
(47) Moularas, C.; Georgiou, Y.; Adamska, K.; Deligiannakis, Y. Thermoplasmonic Heat Generation Efficiency by Nonmonodisperse Core−Shell $Ag^0@SiO_2$ Nanoparticle Ensemble. *J. Phys. Chem. C* **2019**, *123*, 22499−22510.
(48) Naik, G. V.; Shalaev, V. M.; Boltasseva, A. Alternative Plasmonic Materials: Beyond Gold and Silver. *Adv. Mater.* **2013**, *25*, 3264.
(49) Sotiriou, G.; Gass, S.; Pratsinis, S. Hermetically Coated Nanosilver: No Ag^+ Ion Leaching. *Materials Research Society* **2012**, *1386*, 924.
(50) Pratsinis, S.; Mueller, R.; Kammler, H. K.; Madler, L. Controlled Synthesis of Nanostructured Particles by Flame Spray Pyrolysis. *Aerosol Science* **2002**, *33*, 369−389.
(51) Teoh, L.; Amal, R.; Mädler, W. Y. Flame Spray Pyrolysis: An Enabling Technology for Nanoparticles Design and Fabrication. *Nanoscale* **2010**, *2*, 1324.
(52) Sotiriou, G.; Sannomiya, T.; Teleki, A.; Krumeich, F.; Pratsinis, S.Non-Toxic Dry-Coated Nanosilver for Plasmonic Biosensors, *ADVANCED MATERIALS*, 2010.
(53) Teleki, A.; Heine, M.; Krumeich, F.; Akhtar, K.; Pratsinis, S. In Situ Coating of Flame-Made TiO_2 Particles with Nanothin SiO2 Films. *Langmuir* **2008**, *24*, 12553−12558.
(54) Teleki, A.; Akhtar, M. K.; Pratsinis, S. E. The Quality of SiO_2-Coatings on Flame-Made TiO_2-Based Nanoparticles. *J. Mater. Chem.* **2008**, *18*, 3547.
(55) García de Abajo, F. J.; Howie, A. Retarded Field Calculation of Electron Energy Loss in Inhomogeneous Dielectrics. *Phys. Rev. B* **2002**, *65*, 115418.
(56) Palik, E. D.*Handbook of Optical Constants of Solids*; Academic Press, 1998.
(57) Grigoropoulou, G.; Christoforidis, K. C.; Louloudi, M.; Deligiannakis, Y. Structure-Catalytic Function Relationship of SiO_2 -Immobilized Mononuclear Cu Complexes: An EPR Study. *Langmuir* **2007**, *23*, 10407−10418.
(58) Stover, N. M. Diphenylcarbazide as a Test for Chromium. *J. Am. Chem. Soc.* **1928**, *50*, 2363−2366.
(59) Jiang, M.-M.; Chen, H.-Y.; Li, B.-H.; Liu, K.-W.; Shan, C.-X.; Shen, D.-Z. Hybrid Quadrupolar Resonances Stimulated at Short Wavelengths Using Coupled Plasmonic Silver Nanoparticle Aggregation. *J. Mater. Chem. C* **2014**, *2*, 56−63.
(60) Das, S. K.; Khan, Md. M. R.; Parandhaman, T.; Laffir, F.; Guha, A. K.; Sekaran, G.; Mandal, A. B. Nano-Silica Fabricated with Silver Nanoparticles: Antifouling Adsorbent for Efficient Dye Removal,

https://doi.org/10.1021/acs.jpcc.2c07837
J. Phys. Chem. C 2023, 127, 2045−2057

Effective Water Disinfection and Biofouling Control. *Nanoscale* **2013**, *5*, 5549.
(61) Sotiriou, G. A.; Meyer, A.; Knijnenburg, J. T. N.; Panke, S.; Pratsinis, S. E. Quantifying the Origin of Released Ag^+ Ions from Nanosilver. *Langmuir* **2012**, *28*, 15929−15936.
(62) Andriessen, W. T. M.; Groenewege, M. P. Electron Paramagnetic Resonance of Chromium(III) Complexes of the Type Cis-[Cr(2,2'-Bpy)2XY]Z, Cis-[Cr(1,10-Phen)2XY]Z, and Cis-[Cr(Ox)-2XY]Z in Frozen Solutions and Powders. *Inorg. Chem.* **1976**, *15*, 621−626.
(63) Mytych, P.; Cieśla, P.; Stasicka, Z. Photoredox Processes in the Cr(VI)−Cr(III)−Oxalate System and Their Environmental Relevance. *Applied Catalysis B: Environmental* **2005**, *59*, 161−170.
(64) Psathas, P.; Georgiou, Y.; Moularas, C.; Armatas, G. S.; Deligiannakis, Y.*Controlled-Phase Synthesis of $Bi_2Fe_4O_9$ & $BiFeO_3$ by Flame Spray Pyrolysis and Their Evaluation as Non-Noble Metal Catalysts for Efficient Reduction of 4-Nitrophenol*; Powder Technology, 2020.
(65) Peng, H.; Guo, J. Reduction Behavior of Chromium(VI) with Oxalic Acid in Aqueous Solution. *Sci. Rep.* **2020**, *10*, 17732.
(66) Zhou, L.; Swearer, D. F.; Zhang, C.; Robatjazi, H.; Zhao, H.; Henderson, L.; Dong, L.; Christopher, P.; Carter, E. A.; Nordlander, P.; Halas, N. J. Quantifying Hot Carrier and Thermal Contributions in Plasmonic Photocatalysis. *Science* **2018**, *362*, 69−72.
(67) Swearer, D. F.; Robatjazi, H.; Martirez, J. M. P.; Zhang, M.; Zhou, L.; Carter, E. A.; Nordlander, P.; Halas, N. J. Plasmonic Photocatalysis of Nitrous Oxide into N_2 and O_2 Using Aluminum−Iridium Antenna−Reactor Nanoparticles. *ACS Nano* **2019**, *13*, 8076−8086.
(68) Yuan, L.; Lou, M.; Clark, B. D.; Lou, M.; Zhou, L.; Tian, S.; Jacobson, C. R.; Nordlander, P.; Halas, N. J. Morphology-Dependent Reactivity of a Plasmonic Photocatalyst. *ACS Nano* **2020**, *14*, 12054−12063.
(69) Sivan, Y.; Baraban, J.; Un, I. W.; Dubi, Y. Comment on "Quantifying Hot Carrier and Thermal Contributions in Plasmonic Photocatalysis. *Science* **2019**, *364*, No. eaaw9367.
(70) Zhou, L.; Swearer, D. F.; Robatjazi, H.; Alabastri, A.; Christopher, P.; Carter, E. A.; Nordlander, P.; Halas, N. J. Response to Comment on "Quantifying Hot Carrier and Thermal Contributions in Plasmonic Photocatalysis. *Science* **2019**, *364*, No. eaaw9545.
(71) Mascaretti, L.; Naldoni, A. Hot Electron and Thermal Effects in Plasmonic Photocatalysis. *J. Appl. Phys.* **2020**, *128*, 041101.
(72) Baffou, G.; Bordacchini, I.; Baldi, A.; Quidant, R. Simple Experimental Procedures to Distinguish Photothermal from Hot-Carrier Processes in Plasmonics. *Light Sci Appl* **2020**, *9*, 108.

https://doi.org/10.1021/acs.jpcc.2c07837
J. Phys. Chem. C 2023, 127, 2045−2057